

Harnessing Photoredox Cascade to Enhance Photodynamic Oncotherapy by Nanoformulated Macrocyclic Photosensitizer

Qin Liu¹, Zhuo Lei¹, Fangjian Shang¹, Xiaoyun Dong¹, Erwen Yang¹, Ying-Ming Zhang^{1*}, Qilin Yu², Xiufang Xu¹ & Yu Liu^{1*}

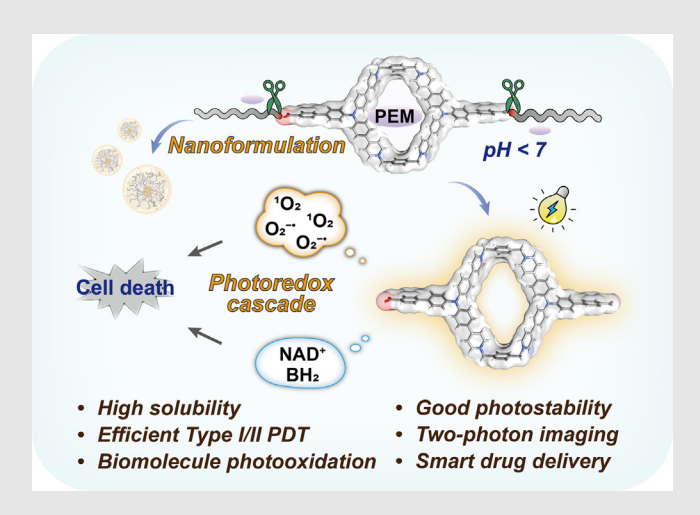
¹College of Chemistry, State Key Laboratory of Elemento-Organic Chemistry, Collaborative Innovation Center of Chemical Science and Engineering (Tianjin), Nankai University, Tianjin 300071, ²Key Laboratory of Molecular Microbiology and Technology, Ministry of Education, Department of Microbiology, College of Life Sciences, Nankai University, Tianjin 300071

*Corresponding authors: ymzhang@nankai.edu.cn; yuliu@nankai.edu.cn

Cite this: CCS Chem. 2025, Just Published. DOI: 10.31635/ccschem.025.202505567

Optically active nanoagents hold a dominant position in advanced phototheranostics, but there remain challenges in structural optimization and performance maximization for biomedical applications. Herein, a π -extended triphenylamine-containing tetracationic macrocycle (1.4CI) is rationally designed and fully exploited as a versatile photosensitizer (PS) for tumor ablation. The reactive oxygen species (102 and O2-*) can be simultaneously produced by 1 · 4Cl, and the 102 quantum yield can reach up to 265%, which overwhelms most known PSs. Also, 1 · 4Cl can trigger the photoredox cascade with nicotinamide adenine dinucleotide and tetrahydrobiopterin, by which these biomolecules are photooxidized and the intracellular redox balance is disrupted. The molecular dimension of crystalline 1 · 4Cl (17.0 \times 15.3 Å²) is appropriate for the noncovalent communication with pemetrexed (binding constant > 10⁶ M⁻¹). Strikingly, the PEGylation via hydrazone bond (1-PEG) can not only retain the compelling photophysical properties, but also endow the parental 1.4Cl with desired environmentally responsive characteristics and prolonged retention in tumor tissues. Consequently,

the PEM@1-PEG nanoformulation achieves a high mortality rate of 77.2% in the A549 cells and a good antitumor efficacy of 93.4% in the murine model. To the best of our knowledge, this is the first such example of an all-in-one macrocyclic PS for holistic phototherapy.



Keywords: macrocyclic chemistry, molecular recognition, photosensitizer, environmental responsiveness, supramolecular phototherapy

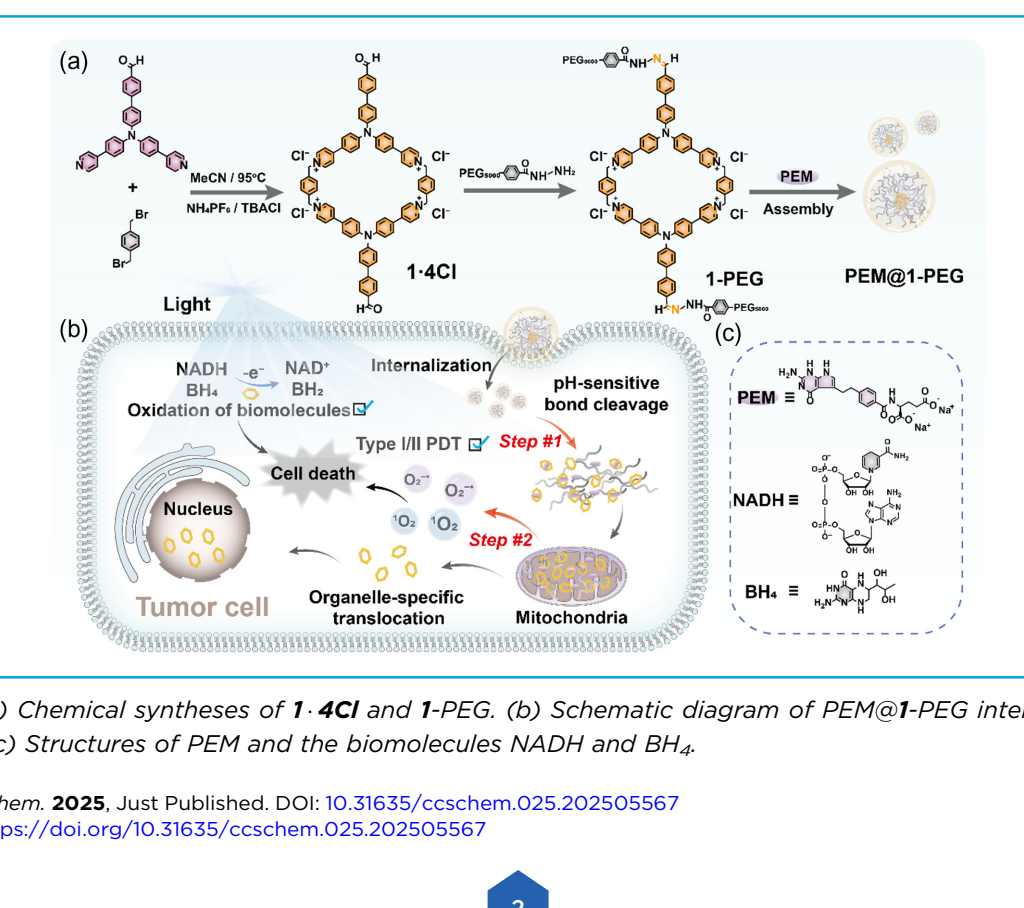


Introduction

Photomediated supramolecular nanotheranostics, including photoacoustic imaging, photothermal therapy, and photodynamic therapy (PDT), mostly relies on the precise manipulation of the photophysical properties of optical agents.¹⁻⁸ In this context, PDT with photosensitizers (PSs) that produce reactive oxygen species (ROS) has recently been explored as an appealing modality for disease treatments because of its minimal invasiveness, high selectivity, and low systemic toxicity.9-15 Frequently encountered PSs, such as porphyrins and phthalocyanines, are π -conjugated organic dyes with solid planar structures, which are always subjected to self-aggregation-caused quenching in photoluminescence and an inherent deficiency in ROS production. 16,17 This situation would be further exacerbated in complex biological fluids and a hypoxic tumor microenvironment. To meet the ever-growing demand for well-adjusted photoactive nanoconstructs and alleviate the high oxygen dependence for ROS generation in deep-seated tumor tissues, there is an urgent pursuit of more reliable photodynamic agents for a wide range of biomedical applications. Under such circumstances, in addition to the conventional ROS generation merely achieved by the electron/energy transfer between PSs and triplet oxygen molecules (i.e., Type-I/II pathways), 18-20 the PS-triggered photochemical reactions involving some intracellularly abundant biomolecules (i.e., Type-III pathway), 21,22 such as ribonucleic acid and pyruvic acid, can severely interfere with the key metabolic processes in malignant cells and thoroughly

reduce the dependency on external oxygen supply. This protocol eventually results in superb photocytotoxicity and excellent in vivo antitumor efficacy, highlighting the promising prospects for modern phototherapy. However, to unleash the photodynamic potentials of a given PS, there is no report on the efficient ROS production and PDT improvement simultaneously through Type-I/II/III pathways, to the best of our knowledge.

In the realm of supramolecular chemistry, the emergence of macrocyclic compounds opens up an alternative or even powerful avenue for high-performance phototheranostics. On one hand, superior to the de novo molecular design of new types of PSs, some classic cavity-bearing macrocyclic hosts, such as cyclodextrins and cucurbiturils, can directly accommodate and separate the known PS guests as a single-molecule form via host-guest complexation without altering their chemical structures, thus mitigating undesired self-aggregation and boosting photophysical outcomes.²³⁻²⁸ On the other hand, superior to their flexible acyclic counterparts, the rigidified macrocyclic products arising from the cyclization process allow for the conformational immobilization of $\pi\text{-conjugated}$ segments via spatially mutual restriction, which can facilitate the enhancement of photosensitizing effect, especially in the intermolecularly aggregated state.²⁹⁻³¹ In this regard, however, the confinement of small-molecule π -aromatic precursors into macrocyclic PSs typically necessitates elaborate selection of suitable chromophores and stringent control over the cavity size, which may lead to tedious chemical synthesis with limited options. Therefore, it is highly imperative to develop



Scheme 1 | (a) Chemical syntheses of 1 · 4Cl and 1-PEG. (b) Schematic diagram of PEM@1-PEG internalization into tumor cells. (c) Structures of PEM and the biomolecules NADH and BH₄.



macrocycle-type optical agents that can reconcile photosensitizing activity with molecular recognition ability, while guaranteeing photostability, biocompatibility, ease of operation, environmental responsiveness, and PDT effectiveness.

We thus hypothesize that the chemical structures of macrocyclic PSs can be further optimized by the π -extension of a molecular skeleton to maximize the photodynamic performance, and functional anchoring points can be introduced to allow postsynthetic modification and increase the functionality of supramolecular nanosystem. With this in mind, in the present work, by combining the innate merits of inclusiveness of a built-in cavity and the structural diversity of electron-rich arenes. a π -extended triphenylamine-bearing three-dimensional tetracationic macrocycle (1.4Cl) was created by a onestep cyclization reaction (Scheme 1a-c). The adaptable nanocavity of $1 \cdot 4CI$, which is encircled by multiple π aromatic rings and positive charges, exhibited strong molecular binding affinity toward pemetrexed (PEM), a clinically approved chemotherapeutic drug. Illumination of $1 \cdot 4CI$ generated singlet oxygen (${}^{1}O_{2}$) and superoxide anion (O2-*) as the main ROS with extraordinarily high quantum yield. More remarkably, by harnessing the 1.4CI-involved photoredox cascade reactions, nicotinamide adenine dinucleotide (NADH) and tetrahydrobiopterin (BH₄), as the essential biomolecules, were photooxidized to give their deprotonated products in cells. The PEGylated 1 · 4Cl (1-PEG) via pH-sensitive acylhydrazone linkage showed targeted fluorescence imaging in tumors and prolonged circulation in blood. In this way, the drug-loaded binary nanoformulation (PEM@1-PEG) exhibited synergistic chemo-photodynamic therapeutic effects. To be envisioned, such a macrocyclic PS with modifiable molecular structure and tunable photodynamic activity may hold great promise in attaining more advanced photoactive bioagents.

Experimental Methods

Data fitting methods

Taking $1 \cdot 4CI$ and PEM as an example, the calculation of binding constant (K_S) can be determined using a nonlinear least squares method by the following equation.³²

$$\begin{split} \Delta F &= \frac{1}{2} \left\{ \alpha ([H]_{0} + [G_{0}] + 1/K_{S}) \right. \\ &\left. \pm \sqrt{\alpha^{2} ([H]_{0} + [G]_{0} + 1/K_{S})^{2} - 4\alpha [H]_{0} [G]_{0}} \right\} \end{split}$$

where $[G]_0$ and $[H]_0$ refer to the total concentration of $\mathbf{1}\cdot\mathbf{4Cl}$ and PEM, respectively; α is the proportionality coefficient, which may be taken as a sensitivity factor for the fluorescence change; and ΔF denotes the change in the fluorescence spectrum of $\mathbf{1}\cdot\mathbf{4Cl}$ upon stepwise addition of the PEM.

Detection of reactive oxygen species production with 2',7'-dichlorodihydrofluorescein

We used 2',7'-dichlorodihydrofluorescein (DCFH) as an ROS probe to detect ROS generation in a solution. When ROS was generated, DCFH was oxidized, leading to an increase in fluorescence at 526 nm. 1·4CI, 1-PEG, or PEM@1-PEG and DCFH were mixed in dark conditions and then irradiated with white light for various durations. The fluorescence intensity at 526 nm was recorded. The blank group only added DCFH without PSs.

Detection of reactive oxygen species production with dihydrorhodamine 123

We employed dihydrorhodamine 123 (DHR123) as an indicator for detecting ROS in solution. When ROS was generated, DHR123 underwent oxidation, resulting in the emission of strong fluorescence centered at 528 nm. 1·4Cl, 1-PEG, or PEM@1-PEG and DHR123 were mixed in dark conditions and then irradiated with white light for various durations. Changes in fluorescence at 528 nm were monitored. The blank group only added DHR123 without PSs.

Detection of ¹O₂ production with 9,10anthracenediyl-bis(methylene)-dimalonic acid

We used compound 9,10-anthracenediyl-bis(methylene)-dimalonic acid (ABDA) as a probe and Rose Bengal (RB) as a standard to detect 1O_2 . When 1O_2 was generated, ABDA underwent oxidation, the UV-vis absorbance intensity of ABDA gradually decreased at 378 nm. **1** · **4Cl** or RB and ABDA were mixed in dark conditions and then irradiated with white light for various durations. The blank group only added ABDA without PSs. Changes in absorption at 378 nm were measured by UV-vis spectroscopy. Singlet oxygen quantum yield was calculated by the following equation:²⁹

$$\phi_{\rm G} = \phi_{\rm ST} \frac{k_{\rm G}}{k_{\rm ST}} / \frac{A_{\rm G}}{A_{\rm ST}}$$

where $k_{\rm G}$ and $k_{\rm ST}$, respectively, represent the decomposition rate constants of ABDA with PS (G) and RB (ST). $A_{\rm G}$ and $A_{\rm ST}$ represent the light absorbed by PS (G) and RB (ST), respectively, which are determined by integration of the areas under the absorption bands in the wavelength range of 400–600 nm. $\Phi_{\rm ST}$ is the $^{1}{\rm O}_{2}$ quantum yield of RB, which is 0.75 in water.

Detection of O₂⁻• production with dihydroethidium

We utilized dihydroethidium (DHE) as a specific probe for detecting the generation of $O_2^{-\bullet}$. When $O_2^{-\bullet}$ was produced, DHE was oxidized, leading to the formation



of ethidium, which intercalated into DNA and emitted strong fluorescence at approximately 580 nm. 1·4Cl, 1-PEG, or PEM@1-PEG were mixed with ctDNA and DHE in dark conditions and then irradiated with white light for various durations. The fluorescence emitted from the sample at 580 nm was measured. The blank group only added DHE without PSs.

Detection of O₂⁻• production with electron paramagnetic resonance spectroscopy

We utilized electron paramagnetic resonance (EPR) spectroscopy to detect the generation of ${\rm O_2}^{-\bullet}$. For this purpose, we employed 5,5-dimethyl-1-pyrroline *N*-oxide (DMPO) as a spin-trap agent specifically for ${\rm O_2}^{-\bullet}$. The 1 mg/mL sample was prepared in methanol and ultrasonic dispersion was performed for 5 min. A 30 μ L sample was added into 30 μ L DMPO (100 mM methanol as solvent) and mixed. The mixture was illuminated/not illuminated with a xenon lamp. Then, a certain amount of mixture was absorbed with a capillary, sheathed quartz tube and put into the EPR sample chamber for superoxide free radical test.

NADH oxidation experiments

The $1\cdot 4\text{Cl}$, 1-PEG, or PEM@1-PEG solution containing NADH treated with or without N $_2$ degassing was under white-light irradiation for different time intervals. When NADH was oxidized, the absorbance of NADH at 340 nm decreased, and the absorbance at 340 nm was recorded. The blank group only added NADH without PSs.

BH₄ oxidation experiments

The $1\cdot 4\text{Cl}$, 1-PEG, or PEM@1-PEG solution containing BH₄ treated with or without N₂ degassing was under white-light irradiation for different time intervals. When BH₄ was oxidized, the absorbance of BH₄ at 294 nm decreased and the absorbance at 294 nm was recorded. The blank group only added BH₄ without PSs.

Cyclic voltammetry measurement

Cyclic voltammetry (CV) experiments were carried out with a three-electrode device. A platinum-carbon composite electrode, a platinum wire electrode, and an Ag/AgCl electrode were employed as the working, auxiliary, and reference electrodes, respectively. The measurement was performed in a solution of acetonitrile containing 0.1 M tetrabutylammonium hexafluorophosphate as the electrolyte.

The measurement of photocurrent responses

The photocurrent responses experiment was carried out using a three-electrode setup. The working electrode

consisted of a carbon paper electrode attached with the PS, while a platinum wire electrode and an Ag/AgCl electrode were employed as the auxiliary and reference electrodes, respectively. The measurements were conducted in 0.1 M sodium sulfate solution. The experimental device used a xenon lamp illumination system with an intensity of 220 mW/cm².

Cell culture

Human carcinoma A549 cell line was obtained from the Institute of Basic Medical Science, Chinese Academy of Medical Science. A549 cells were cultured in a cell incubator with Dulbecco's modified Eagle's medium/F-12 nutrient medium containing 10% fetal bovine serum and 1% penicillin-streptomycin under 5% CO₂ at 37 °C.

Study on the internalization of photosensitizers

We assessed the intracellular uptake time of the PS by flow cytometry. A549 cells were cultured in a 6-well cell culture plate and allowed to incubate for 24 h. Then, the existing medium was substituted with fresh culture medium containing PS. We measured intracellular fluorescence intensity at different time intervals.

Detection of reactive oxygen species and O₂⁻• generation in living cells

A549 cells were seeded in confocal dishes and allowed to cultivate for 24 h. Then, the A549 cells were treated with 1.4Cl or 1-PEG and incubated at 37 °C for 12 h. Subsequently, the cells were washed three times with phosphate-buffered saline (PBS) (0.01 M) and the culture medium, 1.0 μM DCFH diacetate (DCFH-DA) or DHE, was added to detect the reactive oxygen or ${\rm O_2}^{-\bullet}$ radical. The cells were incubated for 30 min to allow for the probe uptake. After this incubation, the culture medium was removed and the cells were washed three times with PBS buffer. Then, the cells were irradiated with a xenon lamp with an intensity of 220 mW/cm² for 5 min. The cells were observed via confocal laser scanning microscope (CLSM) promptly. For DCFH, the excitation filter was 488 nm, and the emission was 510-540 nm. For DHE, the excitation filter was 559 nm, and the emission range was 570-630 nm.

Study on cell cytotoxicity

The A549 cells were seeded into a 96-well plate for 24 h, and then the medium was replaced with 100 μ L fresh culture medium containing **1** · **4Cl**, **1**-PEG, or PEM@**1**-PEG at different concentrations. The cells were incubated in the dark for 48 h. After that, the cells were exposed to the 450 nm light-emitting diode light (10 mW/cm²). Then,



the cells were continuously cultured for another 3 h. The culture medium was removed after repeated washing with PBS three times, and then fresh culture medium was added. The cell viability was assessed by the cell-counting kit-8 (CCK-8). The plate was then read by a microplate reader at a wavelength of 450 nm, and the assessment of dark solitude omitted the lighting step. Each concentration condition was measured three times.

Study on organelle colocalization

A549 cells were seeded onto a laser confocal dish and cultivated for 24 h. Then, the A549 cells were treated with 1 · 4Cl, 1-PEG, or PEM@1-PEG and incubated at 37 °C for 12 h. The culture medium was removed and washed with PBS three times, and fresh culture medium was added. Subsequently, Mito-Tracker Green was added to stain the mitochondria at 37 °C for 30 min. After that, the cells were repeatedly washed with PBS three times and the nucleus was stained by 4',6-diamidino-2-phenylindole (DAPI) for 30 min at 37 °C. After repeated washing with PBS three times, the cells were observed directly via CLSM. For Mito-Tracker Green, the excitation filter was 488 nm, and the emission was 510-540 nm. For DAPI, the excitation filter was 405 nm, and the emission was 420-450 nm. For 1 · 4Cl, 1-PEG, or PEM@1-PEG, the excitation filter was 405 nm, and the emission was 600-700 nm. The fluorescence emission spectrum of 1 · 4Cl, 1-PEG, or PEM@1-PEG exhibited a broad emission band ranging from 470 to 750 nm. To avoid overlapping with the fluorescence of Mito-tracker Green, only the fluorescence in the 600-700 nm was collected in the confocal microscopic images.

Evaluation of cellular mitochondria membrane potential

In order to detect the changes of mitochondrial membrane potential of A549 cells after different treatments, JC-1 was used as a specific probe. A549 cells were seeded onto a laser confocal dish and cultivated for 24 h. Then, the A549 cells were incubated with 1·4Cl, 1-PEG, or PEM@1-PEG and incubated at 37 °C for 12 h. Then, the cells were washed three times with PBS buffer solution and stained with JC-1 at 37 °C for 20 min. After carefully washing, the cells were observed via CLSM immediately.

In vivo imaging

Tumor imaging in vivo was studied with a subcutaneous A549 tumor model in the immunodeficient BALB/c female mice. The tumor-bearing mice were intravenously injected of 1·4Cl or 1-PEG. Then, the fluorescence was recorded at 18 h with an in vivo imaging system (IVIS) Spectrum imaging system. The excitation wavelength

was 450 nm, and in vivo spectral imaging from 500 to 750 nm (with 10 nm steps) was carried out.

In vivo photodynamic therapy experiment

An in vivo PDT study was performed by using A549 tumor-bearing mice. A549 cells were inoculated into immunodeficient mice 14 days in advance. Then, the mice were divided into six different groups for treatment: Group I: PBS intravenously injection without irradiation; Group II: PBS intravenously injection with irradiation; Group III: 1-PEG intravenously injection without irradiation; Group IV: 1-PEG intravenously injection with irradiation; Group V: PEM@1-PEG intravenously injection without irradiation; and Group VI: PEM@1-PEG intravenously injection with irradiation. Each group contained three mice. After injection for 18 h, a xenon lamp with an intensity of 220 mW/cm² treatment irradiated the tumor region for 10 min. The effect of the different treatment groups was monitored by measuring tumor size (tumor size = width 2 x length/2) and mice body weight for 14 days after PDT treatment. After 14 days, mice were sacrificed and the tumor growth inhibition (TGI) value was calculated according the following equation:³³

$$TGI = (V_0 - V)/V_0 \times 100\%$$

where V and V_0 represent the volume of tumor in the treatment groups and PBS group, respectively.

In vivo histological analysis

The tumor tissues and the main organs (heart, liver, spleen, lung, and kidney) of the mice in the different groups were collected and fixed in 4% paraformaldehyde, and then, paraffin embedded sectioning was conducted for histological hematoxylin and eosin (H&E) staining. Histopathological images of the tissues were captured using a digital slide scanner.

Results and Discussion

The triphenylamine-bearing precursor π -extended by benzaldehyde and pyridyl moieties was synthesized via a palladium-catalyzed coupling reaction, which subsequently underwent a cyclization reaction with 1,4-bis (bromomethyl)benzene under dilute conditions to give the tetracationic macrocycle 1 · 4Cl (Supporting Information Scheme S1). The chemical structure of 1 · 4Cl was comprehensively characterized (Supporting Information Figures S1-S9), and a crystal of 1 · 4PF₆ was obtained by the solvent volatilization from ethyl ether to acetonitrile solution for 3 days, which was confirmed by X-ray single-crystal structure analysis. As shown in Figure 1a-c, 1 · 4PF₆ was arranged to form a three-dimensional compact structure. Positioned between two macrocyclic rings, the PF₆⁻ anions formed a sandwich-like structure, which



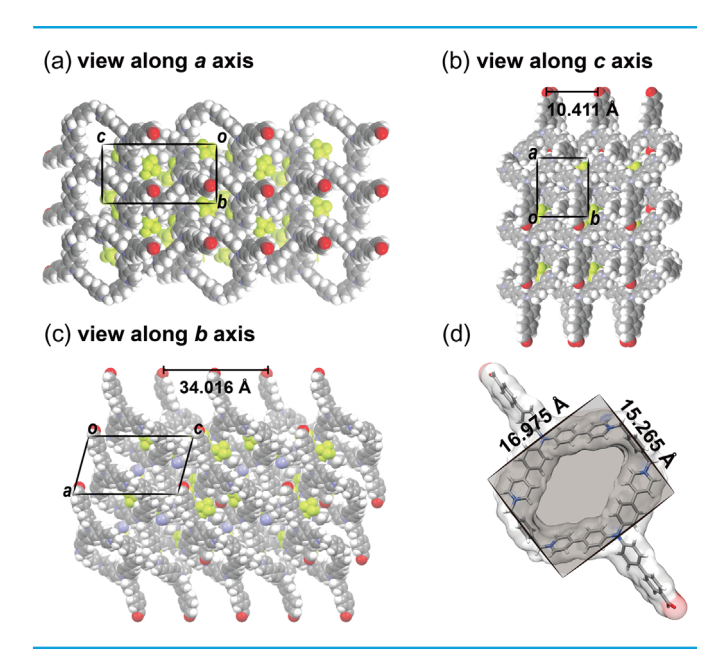


Figure 1 | Space-filling model of the single-crystal X-ray structures of $1 \cdot 4PF_6$ shown along the (a) a-axis, (b) c-axis, and (c) b-axis, respectively. (d) Molecular dimensions measured from the single-crystal structure of $1 \cdot 4PF_6$.

could stabilize the overall arrangement and form the regular channels along the *a* axis (Figure 1a). Due to the twisted conformation of $\mathbf{1} \cdot \mathbf{4PF_6}$, no face-to-face cofacial parallel stacked geometries of π - π interaction were observed; however, the two arms of $\mathbf{1} \cdot \mathbf{4PF_6}$ were intercalated into the adjacent rings, further stabilizing the structure through multiple T-shaped edge-to-face π -stacking interactions. This interlocked structure stabilized the framework by introducing additional anchoring points of weak interactions among the rings. The molecular dimension of $\mathbf{1} \cdot \mathbf{4PF_6}$ was measured as 17.0 × 15.3 Ų, which is appropriate for intermolecular entrapment with some size-matched substrates, as described below (Figure 1d).

Furthermore, the postsynthetic modification on the benzaldehyde site can allow us to improve the whole biocompatibility and curative efficiency through the enhanced permeability and retention effect.³⁴⁻³⁶ Concretely, the predesigned molecular skeleton of 1.4Cl would be endowed with pH sensitivity under the tumor acidic microenvironment by tethering two polyethylene glycol (PEG) chains via acylhydrazone bond, given that the cleavable PEGylation is believed as a reliable strategy to solve the "PEG dilemma" in drug delivery (Supporting Information Scheme S3 and Figures S12-S14).^{37,38} The ¹H nuclear magnetic resonance (NMR) spectrum showed that the resonance peaks assigned to the hydrazide and aldehyde groups in 1 · 4Cl disappeared, whereas the new ones assigned to the acylhydrazone bond appeared at 8.49 and 11.80 ppm (Supporting Information Figure S15).

Moreover, the introduction of two PEG arms could also confer the desired amphiphilic assembling ability to the triphenylamine-bearing tetracationic core. As for the **1-** PEG assemblies, the ζ potential was measured as 7.70 mV, and an average hydrodynamic diameter of approximately 190 nm with uniform size distribution was obtained by means of dynamic light scattering measurement, which was basically consistent with the results observed from the transmission electron microscopic image (Supporting Information Figure S16).

To investigate the photophysical properties of the macrocycle, the UV-vis absorption spectra of 1 · 4Cl and 1.4PF6 were recorded in both aqueous and organic media. As can be seen from Supporting Information Figure S17, the macrocycle had a broad UV-vis absorption in the range of 320-550 nm, and the maximum absorption of the macrocycle was 450 and 440 nm in water and acetonitrile, respectively. Moreover, the macrocycle presented very interesting counterion-dependent photoluminescence behaviors. That is, 1.4PF₆ showed a weak fluorescence emission in acetonitrile at 678 nm, while the 1 · 4Cl gave a very strong fluorescence emission in water at 584 nm with the quantum yield up to 14.6% (Supporting Information Figures S18 and S19). The fluorescence emission was augmented as the polarity of the solvent increased, which can be well interpreted from the principle of aggregation-induced emission (AIE). Subsequently, the AIE properties of 1.4Cl were further studied in the mixed solvents. 1 · 4Cl had extremely weak emission in pure organic solution, but its fluorescence emission intensity gradually increased with the increase of the proportion of water in the mixed solution (Supporting Information Figure S20). Surprisingly, the fluorescence emission of 1.4Cl underwent a gradual hypochromatic shift as the polarity of the solvent increased. This phenomenon is in accordance with some known AlEgens, which mainly contribute to the reduced internal polarity of the formed aggregates^{39,40} and the distorted conformation that is adverse to the π -stacking interaction. 41,42 Particularly, due to the highly symmetrical and rigidified molecular structure, 1.4Cl also exhibited two-photon absorption properties upon excitation at 880 nm, which may hold great potential for bioimaging and disease navigation with minimal skin injury (Supporting Information Figure S21).43-45 In addition, the UV-vis absorbance of 1.4Cl showed no obvious change upon light irradiation for 30 min, while RB, a commercially available PS, substantially decreased in only 3.5 min (Supporting Information Figure S22). These results once again corroborate that the macrocyclic confinement plays a crucial role in improving the photostability of $\textbf{1}\cdot\textbf{4CI}.$ Taking advantage of the good photostability of 1 · 4CI, the cleavage of the acylhydrazone bond of 1-PEG was monitored by fluorescence spectroscopy at different pH, giving enhanced fluorescence emission as the pH decreased from 7.4 to 4.0 in solution (Supporting



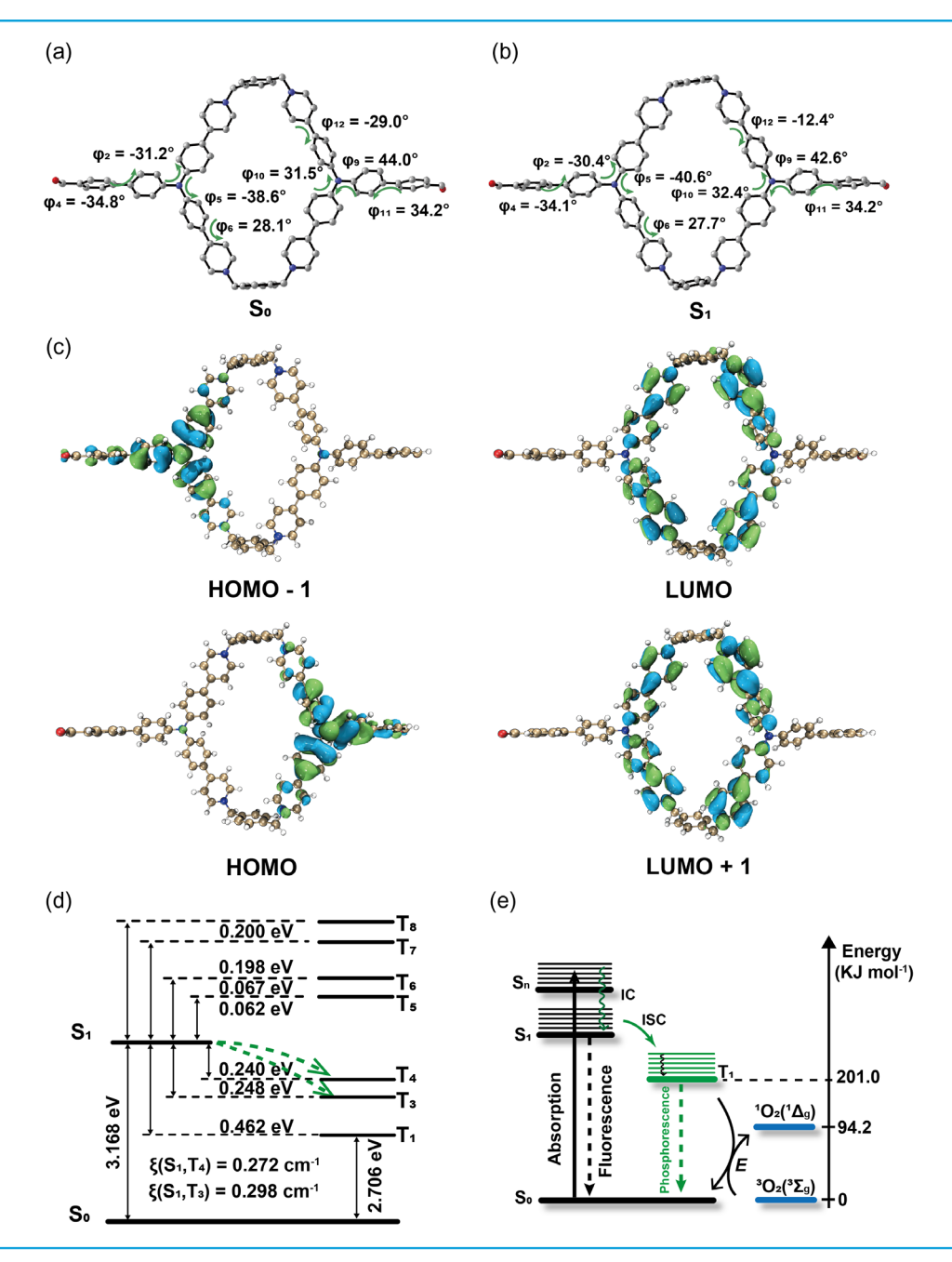


Figure 2 | Optimized geometries and dihedral angles of $1 \cdot 4CI$ in (a) the ground state (S_0); and (b) the first excited singlet state (S_1). (c) Selected molecular orbitals of $1 \cdot 4CI$ with the optimized ground-state geometry in water. (d) Energy-level diagram and SOC coefficients in $1 \cdot 4CI$. (e) The ground state and excited state energy-level diagram of $1 \cdot 4CI$ and O_2 .

Information Figure S23). This is mainly contributed to the loss of bulky PEG chains in the hydrolysis process, which may restore and even strengthen the self-aggregation propensity of parental 1·4Cl. In addition, the fluorescence emission was weakened in the presence of PEM, and we hypothesized that a static quenching occurred between 1·4Cl and PEM, as explained below (Supporting Information Figure S24). Apparently, the multistep fluorescence emission enhancement orthogonally triggered by bond cleavage and drug release may facilitate the

optical bioimaging and disease therapy in the implementation of photodynamic treatment.

Furthermore, to gain deep insights on the photophysical origins, density functional theory (DFT) and time-dependent DFT were applied in the quantum chemical calculations to optimize the molecular structures of $1\cdot 4\text{Cl}$ in the ground (So) and excited states using water as the solvent (Figure 2a,b, Supporting Information Figure S25 and Table S1). The UV-vis absorption spectra and the contribution of different singly excited states (Sn) to



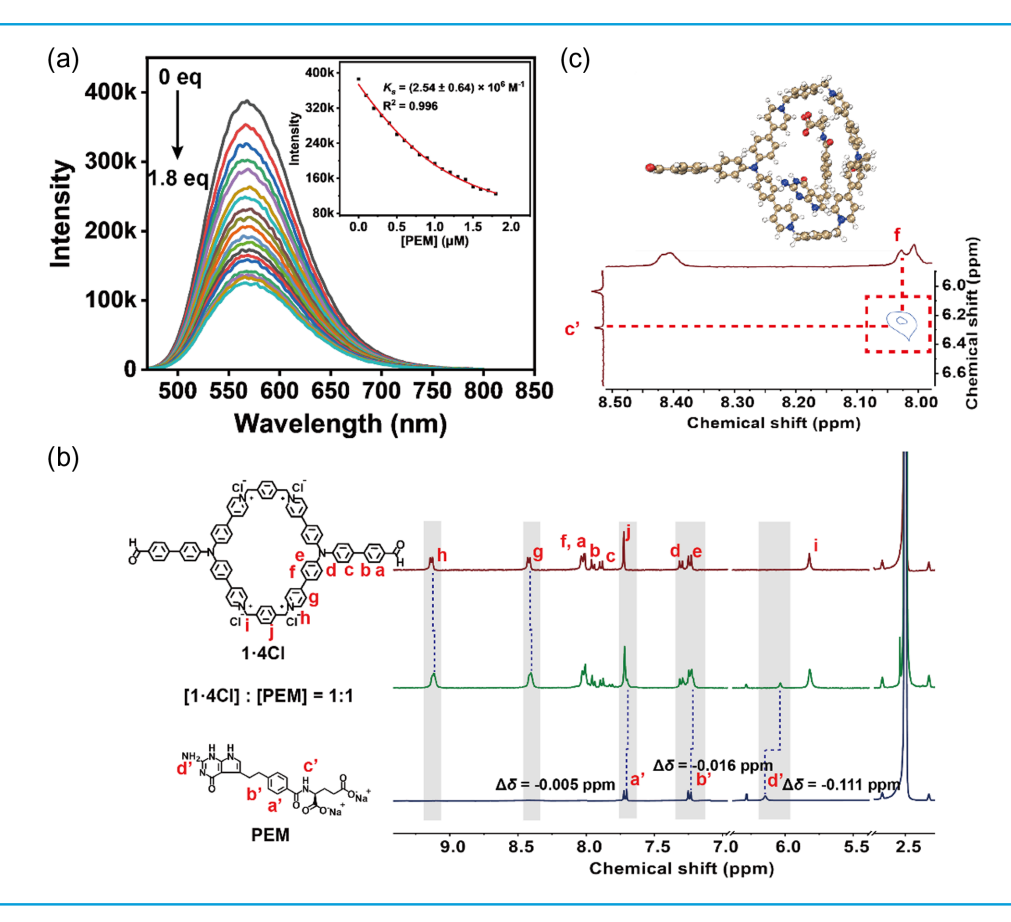


Figure 3 | (a) Fluorescence emission spectra of $1 \cdot 4CI$ upon addition of 0-1.8 equiv of PEM in 4-(2-hydroxyethyl) piperazine-1-ethanesulfonic acid buffer solution. ([$1 \cdot 4CI$] = 1 μ M) Inset: The nonlinear least-squares analyses of the fluorescence emission versus the concentration of PEM to calculate the binding constant (Ks) between $1 \cdot 4CI$ and PEM. (b) ¹H NMR spectra (400 MHz, DMSO-d₆, 298 K) of $1 \cdot 4CI$, PEM, and their binary complex ([$1 \cdot 4CI$] = [PEM] = 0.1 mM). (c) Optimized molecular geometries of PEM@1 and part of ¹H-¹H NOESY spectrum (400 MHz, DMSO-d₆, 298 K) of PEM@1 ([$1 \cdot 4CI$] = [PEM] = 0.1 mM).

the absorption spectra were calculated, implying that the simulated UV-vis absorption spectra at the highest absorption peaks were mainly attributed to the $S_{\text{O}} \rightarrow S_{\text{2}}$ excitation (Supporting Information Figures S26 and S27). Meanwhile, the proportions of the highest occupied molecular orbital (HOMO) - 1 → lowest unoccupied molecular orbital (LUMO) and HOMO → LUMO + 1 excitations were calculated to be 45.8% and 47.8%, respectively.²⁹ As for the HOMO - 1 \rightarrow LUMO and HOMO \rightarrow LUMO + 1 excitation, the electrons were initially localized at the $\boldsymbol{\pi}$ orbitals of the phenyl groups around nitrogen atom and then transferred to the π^{\ast} orbitals of the phenyl and pyridyl groups on the ring skeleton of 1.4Cl. Therefore, the low-energy absorption band in the range of 350-750 nm can be attributed to a joint contribution of the $n \to \pi^*$ and $\pi \to \pi^*$ transitions (Figure 2c). Also, the spin-orbit coupling (SOC) coefficients involving triply excited states (T_n) were calculated to characterize the intersystem crossing (ISC) process in 1.4Cl. The relatively small SOC coefficients [$\xi(S_1, T_3) = 0.298 \text{ cm}^{-1}$ and $\xi(S_1, T_4) = 0.272 \text{ cm}^{-1}$] and large energy gaps $(\Delta E_{\text{S1}\rightarrow\text{T3}} = 0.248 \text{ eV} \text{ and } \Delta E_{\text{S1}\rightarrow\text{T4}} = 0.240 \text{ eV}) \text{ indicate}$

that the fluorescence emission rather than the phosphorescence emission is the favorable radiative pathway in $\mathbf{1\cdot 4Cl}$ (Figure 2d). ^{46,47} It is also found that the calculated triplet energy of $\mathbf{1}$ is higher than the energy gap between the ground O_2 ($^3\Sigma_g$) and the first excited O_2 ($^1\Delta_g$) states (94.2 kJ mol $^{-1}$), which can clarify the experimentally observed phenomena where $\mathbf{1\cdot 4Cl}$ possesses good capability of energy transfer to produce 1O_2 , as described below (Figure 2e). ^{48,49}

PEM, an multitargeted antifolate antineoplastic agent for the treatment of lung cancer and other solid tumors, was selected as the ideal substrate for $\mathbf{1} \cdot \mathbf{4CI}$, on account of the coexistence of aromatic pyrrolopyrimidine and negatively charged glutamic acid residue in PEM, as well as its intended site of action on the mitochondria of cancer cells. Flaving validated the 1:1 binding stoichiometry between $\mathbf{1} \cdot \mathbf{4CI}$ and PEM by a Job plot, fluorescence spectra titration was performed to give the constant $(K_{\rm S})$ between $\mathbf{1} \cdot \mathbf{4CI}$ and PEM up to $(2.54 \pm 0.64) \times 10^6 \,\mathrm{M}^{-1}$ (Figure 3a and Supporting Information Figure S28). Moreover, the fluorescence emission of $\mathbf{1} \cdot \mathbf{4CI}$ was quantitatively quenched upon addition of



PEM, but the emission maximum did not shift, thus indicative of the photoinduced electron transfer process.^{53,54} The static quenching was also confirmed from the timeresolved fluorescence measurements, in which the addition of PEM greatly reduced the fluorescence intensity without changing the fluorescence lifetime of detectable components (Supporting Information Figure S29). Meanwhile, the complexation-induced upfield shifts were observed in the ¹H NMR spectra upon addition of PEM into **1.4Cl** (e.g., $\Delta \delta$ = -0.011 ppm for the pyridyl protons in **1**. **4Cl** and $\Delta\delta$ = -0.016 ppm for the phenyl protons in PEM, respectively, Figure 3b). These upfield shifts arising from the shielding effect of the cavity indicated that the aromatic moieties of PEM might be entrapped by the cavity of 1 · 4Cl. In addition, nuclear overhauser effect spectroscopy (NOESY) was employed to investigate the molecular binding mode. The correlation signals of aromatic protons in 1 · 4Cl and amide proton in PEM manifest the intermolecular noncovalent contact (Figure 3c). The high molecular binding affinity can largely avoid the premature drug release caused by the complex dissociation in the biological environment. Benefiting from the strong complexation, PEM could be readily loaded into the 1-PEG assembly, and the drug encapsulation and loading efficiency were calculated as 55.4% and 7.0%, respectively, by high-performance liquid chromatography. Comparatively, the presence of PEM in the PEM@1-PEG assembly gave larger nanoparticles (around 266 nm) and relatively lower ζ potential (0.56 mV in Supporting Information Figure S30).

Furthermore, to shed more light on the role of macrocyclic structure of 1.4Cl in the molecular recognition with PEM, the mixed $D_2O/DMSO-d_6$ solvent was used to investigate the molecular binding behaviors. It was found that the phenyl ring of PEM underwent more pronounced upfield shifts in D₂O/DMSO- d_6 ($\Delta\delta$ = -0.021 ppm) than in dimethyl sulfoxide (DMSO) ($\Delta\delta$ = -0.005 ppm), probably due to the hydrophobic interaction between 1.4Cl and PEM to some extent (Supporting Information Figure S31). Meanwhile, the noncyclic compound 2 · 2CI was synthesized as reference (Supporting Information Scheme S2, Figures S10 and S11). Only slight fluorescence quenching effect (~25%) of 2 · 2CI was observed upon the addition of PEM, as compared to the cyclic counterpart 1.4Cl (~70%) under the same experimental condition. In addition, smaller K_S value was obtained with relatively larger error in the intermolecular communication between 2. 2CI and PEM (Supporting Information Figure S32). Combined with the above experimental results, it can be inferred that the π -conjugated macrocyclic structure of 1.4Cl with highly dense positive charges is a decisive factor in the molecular binding toward PEM.

After the pH-controlled cleavage of the hydrazone bond and the release of PEM in the first-step response process, the phototriggered ROS generation by the photosensitized 1.4Cl was investigated in the second-step response process (Figure 4a). With continuous light

exposure to 1.4Cl in the presence of two commercial ROS indicators, DCFH and DHR123, fluorescence emission was significantly enhanced, corresponding to the conversion of oxidized products 2',7'-dichlorofluorescein (DCF) and Rhodamine 123 (RH123) upon ROS generation, respectively (Figure 4b-e). Moreover, ABDA was used as the ¹O₂ probe and RB was used as the standard. Surprisingly, the results show that $\mathbf{1} \cdot \mathbf{4CI}$ could efficiently produce ¹O₂ with the quantum yield as high as 265%, whereas the ¹O₂ quantum yield of RB as reference was only 75% (Figure 4f-i and Supporting Information Figure S33). As shown in Supporting Information Table S2, the π -extended macrocyclic PS **1**·**4CI** represents the stateof-the-art photosensitizing material, compared to the previously reported data, to the best of our knowledge. Furthermore, DHE was employed as the O2-• fluorescence probe and its fluorescence intensity gradually increased with the prolonged irradiation time, which showed that $O_2^{-\bullet}$ could be produced by free 1.4Cl (Figure 4j,k). Moreover, electron spin resonance (ESR) spectroscopy was further conducted to verify the O2-• production in methanol by using DMPO as the spintrapping agent. As expected, the ESR spectra showed the characteristic signals of paramagnetic adduct, thereby indicative of the existence of ${\rm O_2}^{-\bullet}$ generated by ${\bf 1}\cdot {\bf 4CI}$ upon light irradiation (Figure 4I). Taken together, the macrocycle 1 · 4Cl is capable of efficient ROS production simultaneously through the Type-I and Type-II mechanisms. Notably, both 1-PEG and PEM@1-PEG possessed high capacity for ${}^{1}O_{2}$ and $O_{2}^{-\bullet}$ generation, thus enabling the stable photodynamic effect in this nanoformulated supramolecular photosensitizing system (Supporting Information Figures S34-S37).

Significantly, 1.4Cl can also react with some biomolecular substrates to form oxidized products under irradiation and then disturb the intracellular redox balance in tumor cells (Figure 5a).55-57 One selected biomolecule is NADH, and considering that it is a key regulator of cellular metabolism, the dynamic changes in the redox states of NADH are crucial for maintaining cellular function and organismal health. $^{\rm 58\text{-}60}$ The oxidation of NADH was confirmed by NMR spectroscopy; that is, new proton peaks assigned to NAD⁺ emerged upon light irradiation in 3 min (Figure 5b). Moreover, the NADH solution was exposed to light in the presence of 1 · 4Cl under normoxic and hypoxic conditions, respectively. With the increased light duration, the characteristic absorption peak at 340 nm gradually decreased, indicating that NADH could be oxidized to NAD⁺ by the 1-mediated electron transfer process even in short supply of O₂ (Figure 5c and Supporting Information Figure S38). 20,61,62 Accordingly, the turnover frequency of NADH oxidation was calculated as 1.86 min⁻¹, highlighting the exceptional photocatalytic efficiency (Supporting Information Figure S39).56,61,63 In addition, the K_S value between $1 \cdot 4CI$ and NADH was accordingly obtained as $(1.73 \pm 0.79) \times 10^5 \,\mathrm{M}^{-1}$ in buffer



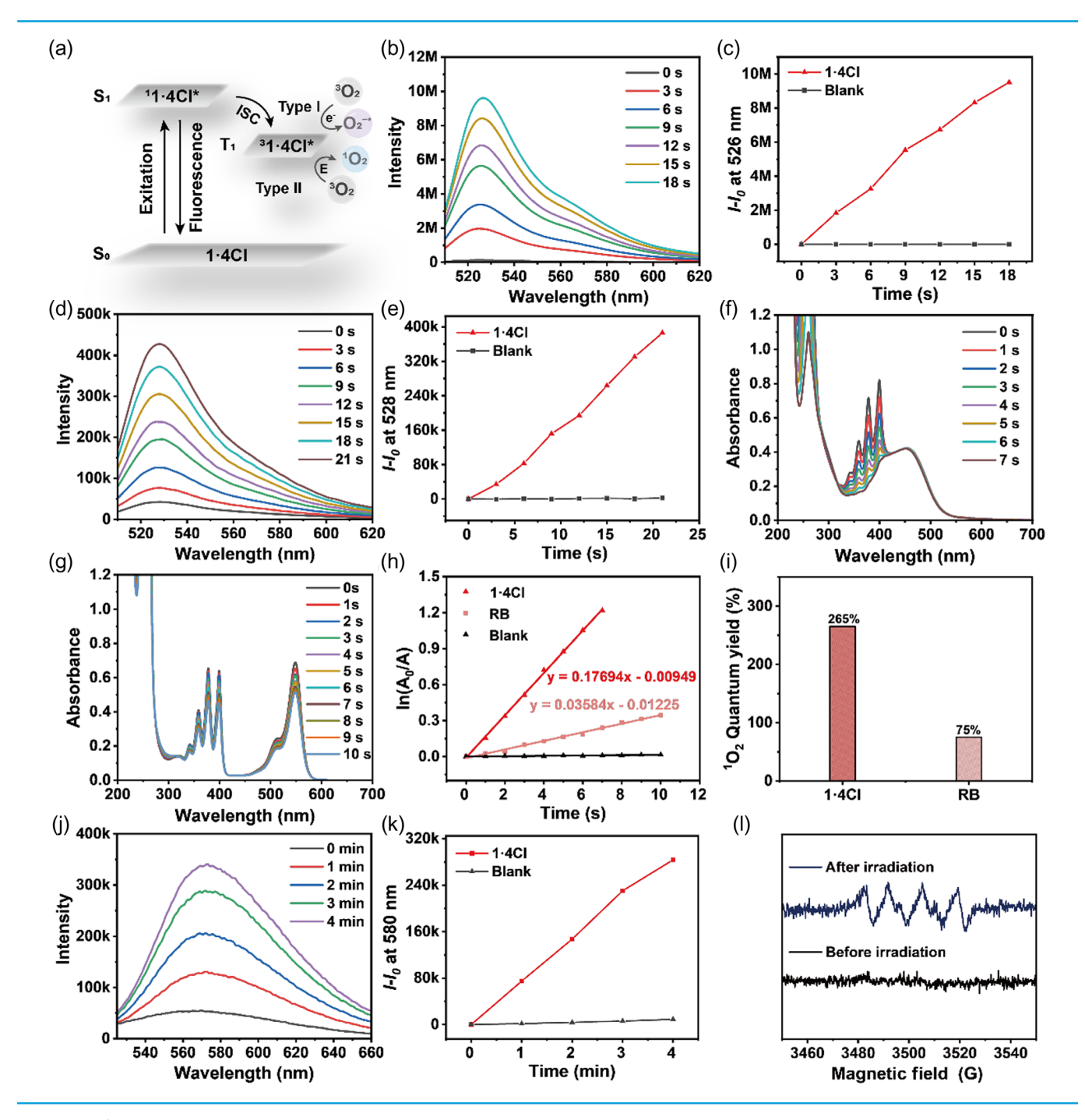


Figure 4 | (a) Schematic illustration of the mechanism of light-induced ROS generation by **1·4Cl**. Fluorescence spectra of (b) DCFH (10 μM) and (d) DHR123 (10 μM) in the presence of **1·4Cl** (1 μM) under white-light irradiation for different time intervals, and their corresponding plots of Δl (1 – l_0) vs time of (c) DCFH at 526 nm and (e) DHR123 at 528 nm. UV-vis spectra of ABDA (50 μM) in the presence of (f) **1·4Cl** (10 μM) and (g) RB (10 μM) under white-light irradiation for different time intervals. (h) Normalized degradation percentages of ABDA at 378 nm in the presence of **1·4Cl** and RB. (i) 1 O₂ quantum yield of **1·4Cl** with reference to the standard RB in aqueous solution. (j) Fluorescence spectra of DHE (40 μM) containing 500 μg mL $^{-1}$ ctDNA in the presence of **1·4Cl** (10 μM) under white-light irradiation for different time intervals, and (k) its corresponding plots of Δl (1 – l_0) vs time of DHE at 580 nm. (l) EPR spectra of O₂^{-•} generated by **1·4Cl** (1 mM) and detected by DMPO (100 mM) in methanol before and after light irradiation.

solution by UV-vis spectroscopy, likely due to the contribution of favorable electrostatic attraction (Supporting Information Figure S40).

The other selected biomolecule is BH₄, which is an important physiologically active substance that plays a variety of key roles in the physiological process.⁶⁴⁻⁶⁶ BH₄



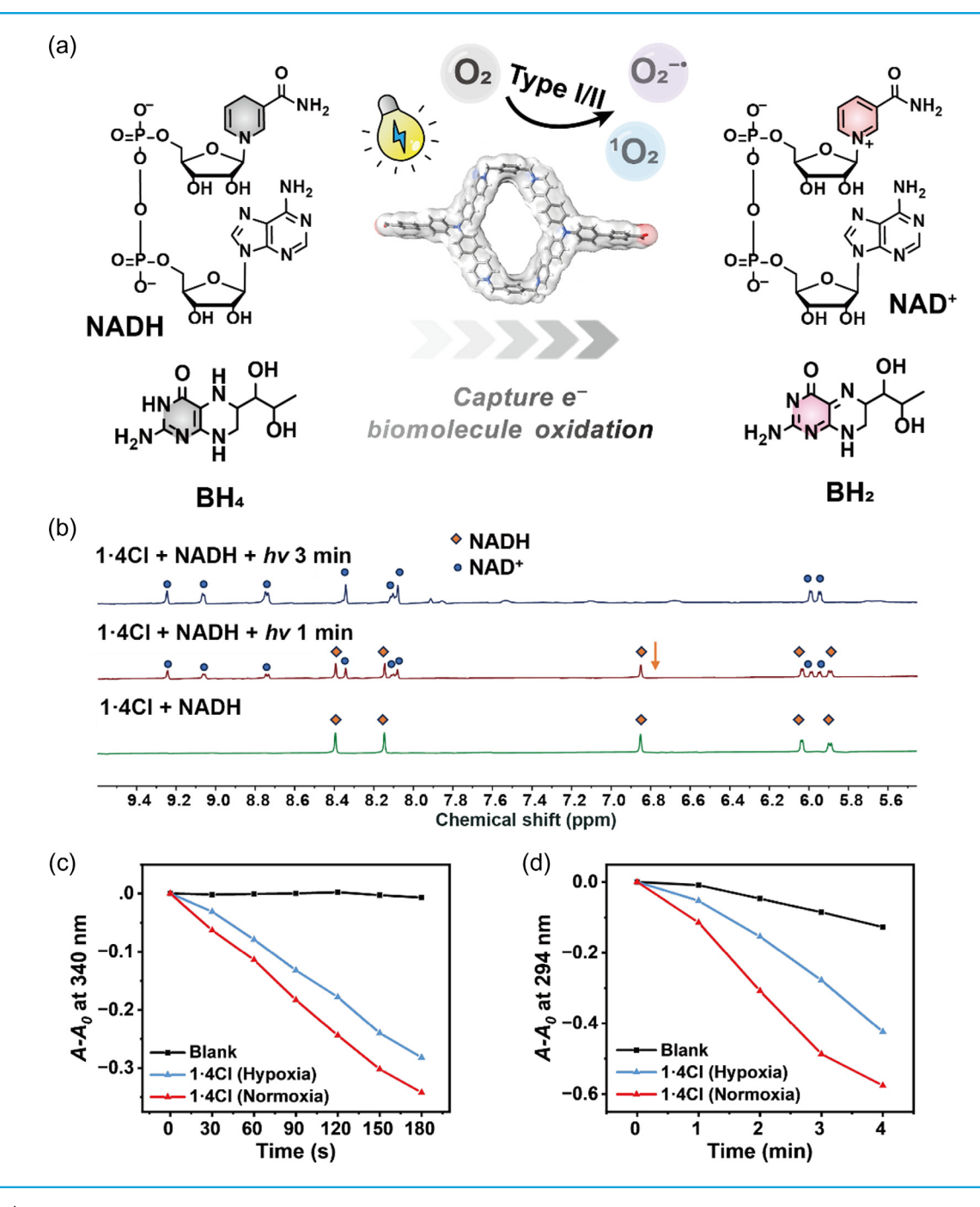


Figure 5 | (a) Schematic illustration of the mechanism of the photooxidation of biomolecules by $\mathbf{1} \cdot \mathbf{4CI}$. (b) ¹H NMR spectra (600 MHz, D_2O , 298 K) of $\mathbf{1} \cdot \mathbf{4CI}$, NADH, and their binary complex ([$\mathbf{1} \cdot \mathbf{4CI}$] = 10 μ M and [NADH] = 100 μ M). UV-vis spectra of (c) NADH (100 μ M) and (d) BH₄ (100 μ M) in the presence of $\mathbf{1} \cdot \mathbf{4CI}$ (10 μ M) under white-light irradiation for different time intervals under the normoxic or hypoxic condition. The solution was degassed with N_2 for hypoxic conditions ($\lambda > 420$ nm, 220 mW/cm²).

is susceptible to oxidative damage and produces BH_2 in the oxidized state, which can reduce of the content of BH_4 in cells and eventually lead to cell metabolic damage and cell death. The UV-vis absorbance decreased at 294 nm in the presence of $1 \cdot 4CI$ by light irradiation in both normoxic and hypoxic conditions (Figure 5d and Supporting Information Figure S41). Meanwhile, the m/z peak assigned to BH_2 was clearly observed at 240.10932

after photooxidation by $1\cdot 4CI$ (Supporting Information Figure S42). These results jointly demonstrate that $1\cdot 4CI$ can directly induce the photooxidation of NADH and BH₄ without ROS consumption, which is believed to be a complimentary factor for the Type-I PDT. ⁶⁷⁻⁶⁹ Also, the photocatalytic performances of 1-PEG and PEM@1-PEG were evaluated (Supporting Information Figures S38 and S41).



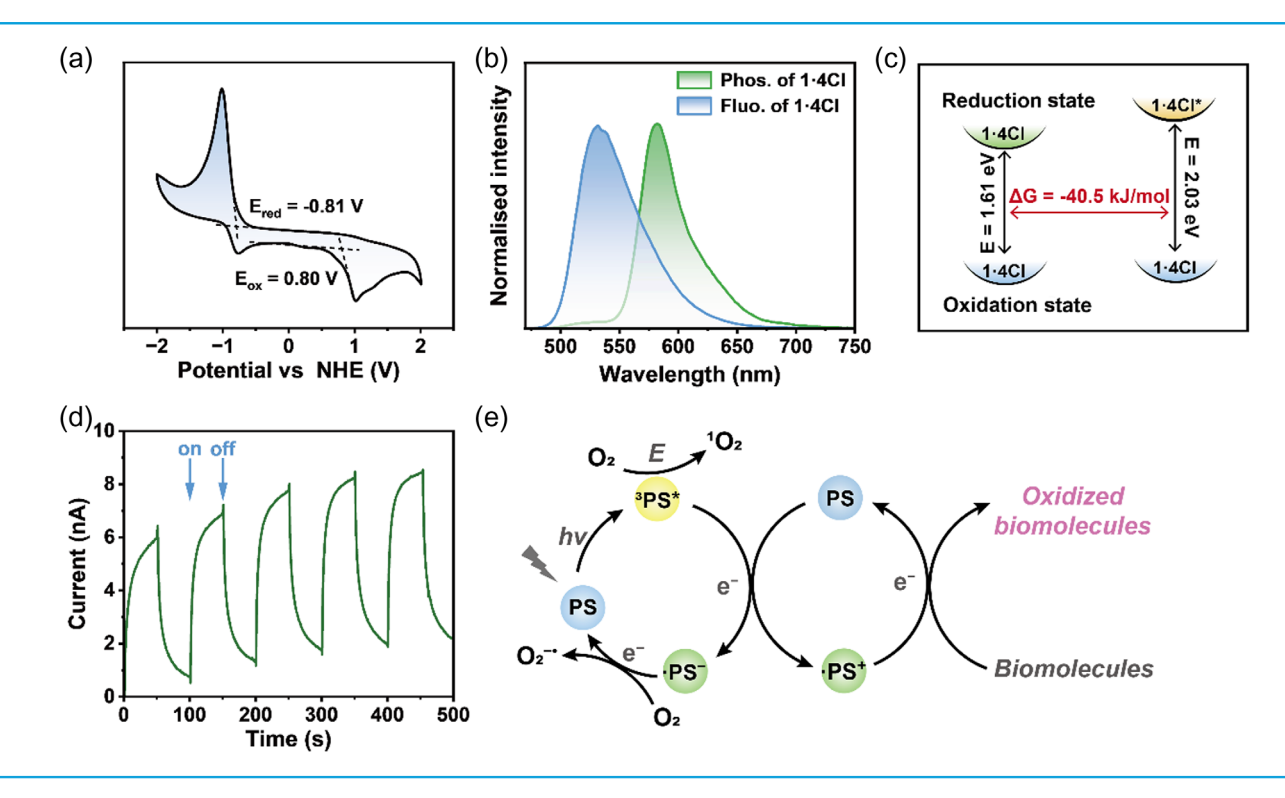


Figure 6 (a) Cyclic voltammogram of $1 \cdot 4CI$. (b) Normalized photoluminescence spectra and phosphorescence emission spectra at 79 K. (c) Calculated Gibbs free energy of electron transfer between ground and excited states in $1 \cdot 4CI$. (d) Photocurrent responses of $1 \cdot 4CI$ with the time intervals of 50 s. (e) Schematic illustration of the photoinduced biomolecule oxidation and ROS generation.

To explore the mechanism underlying ROS generation and biomolecule oxidation, electrochemical experiments and calculations were conducted. The oxidation (E_{ox}) and reduction potentials (E_{red}) of $1 \cdot 4CI$ as PS were measured as 0.80 and -0.81 V, respectively, by CV (Figure 6a). The phosphorescence emission peak of 1. 4CI was measured by recording the time-delay spectra at 79 K, and accordingly, the $E_{\rm T}$ was calculated to be 2.13 V (Figure 6b). Therefore, the Gibbs free energy ($\Delta G_{\rm eT}$) of photoinduced electron transfer could be determined as -40.5 kJ/mol by combining the redox potential with the excitation energy of the macrocyclic PS 1 · 4CI, indicative of the thermodynamic energy barrier for the intermolecular electron transfer process (Figure 6c). The photocurrents of 1 · 4Cl were also measured to assess their ability to create electron holes under light irradiation. The results provide compelling evidence that 1.4Cl could generate photocurrents and possesses the ability of charge separation upon switching the light input (Figure 6d).

After scrutinizing these data, the complete photophysical pathways may be described as follows: $1\cdot 4CI$ is initially photoexcited from the ground state (PS) to the singly excited state ($^{1}PS^{*}$) and then to the triply excited state ($^{3}PS^{*}$) via the ISC transition. On one hand, $^{3}PS^{*}$ transfers energy to the surrounding $^{3}O_{2}$ and produce $^{1}O_{2}$. On the other hand, $^{3}PS^{*}$ undergoes electron transfer

with PS to generate PS⁺• and PS⁻•. The latter species further reacts with 3O_2 to produce O_2^{-} •, while PS⁺• captures electrons and gets involved in the oxidation reaction with the biomolecules (e.g., NADH and BH₄). The plausible photochemical reaction mechanisms are proposed in Figure 6e.

Enthusiastic about the findings of highly efficient ROS generation and the biomolecule oxidation in inanimate milieu, the photoinduced cytotoxicity by 1 · 4Cl was further evaluated in the cell environment. First, the cellular uptake behaviors were assessed by flow cytometry, showing that 1.4Cl could be efficiently internalized by the human lung adenocarcinoma (A549) cells. The peak reached in 6 h and 1 · 4Cl could be retained in cells for at least 24 h (Supporting Information Figure S43). As for **1-PEG**, the fluorescence population rapidly increased in 6 h and leveled off in 12 h, mainly due to the stepwise cleavage of acylhydrazone bond in cells (Supporting Information Figure S44). In addition, the intracellular fluorescence slowly increased after loading PEM into 1-PEG, which results from the in-situ drug release and bond cleavage in the first-step response process (Supporting Information Figure S45).

Next, the subcellular localization of $1 \cdot 4CI$ was visualized using laser confocal microscopy. As shown in Figure 7a, when the A549 cells were incubated with $1 \cdot 4CI$ for 12 h and stained with the Mito-Tracker dye,



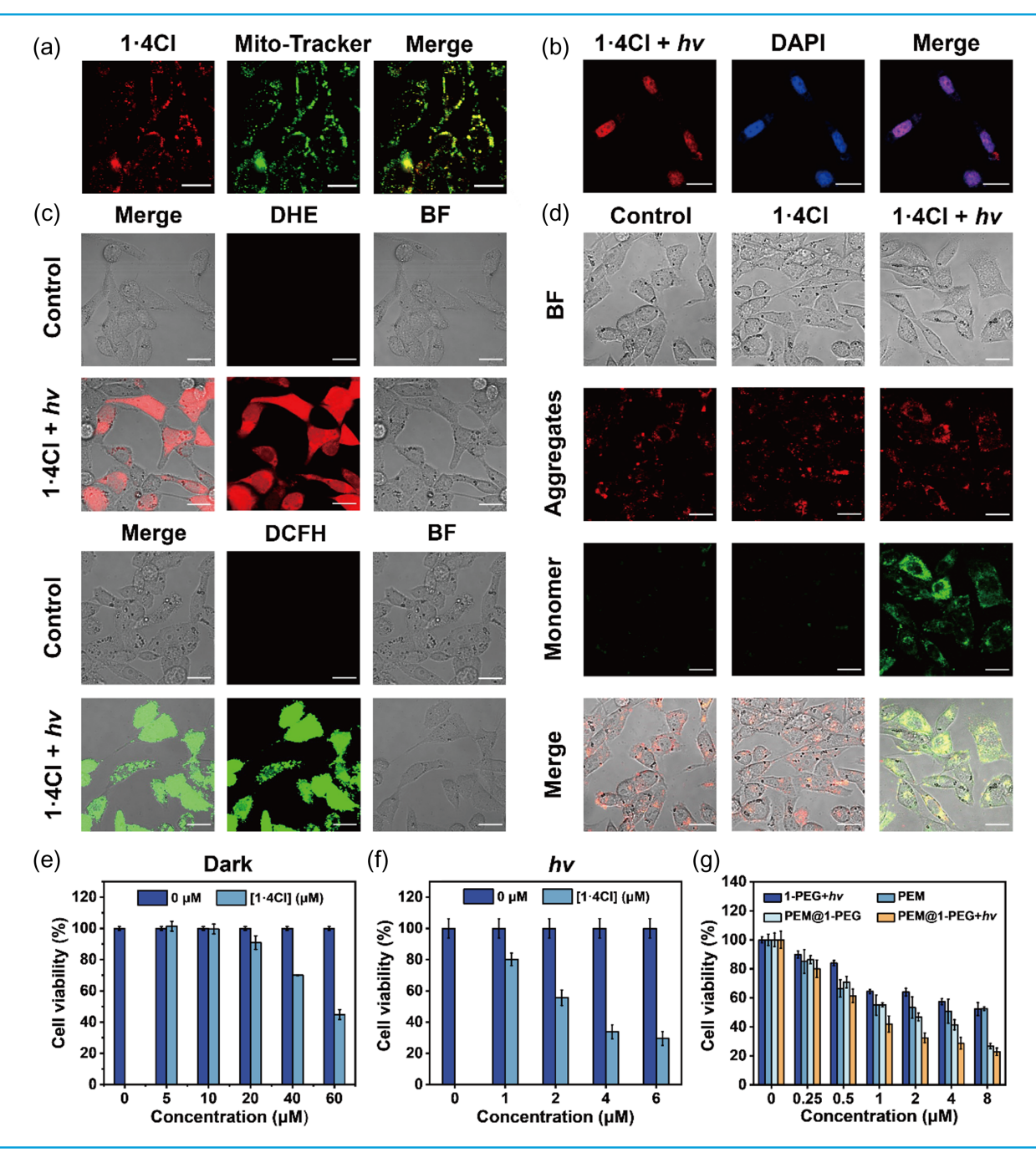


Figure 7 | (a) Mitochondria and (b) nuclei colocalization images in the living A549 cells upon coincubation with $1 \cdot 4CI$. Mito-Tracker (green) and DAPI (blue) were used to stain mitochondria and the nucleus, respectively. The fluorescence of $1 \cdot 4CI$ was red. (c) Intracellular $O_2^{-\bullet}$ and ROS production of $1 \cdot 4CI$ detected by DHE and DCFH under light irradiation. (d) Confocal fluorescence images of JC-1-stained A549 cells with different treatments. The scale bar is 20 μ m ([$1 \cdot 4CI$] = 2μ M, $\lambda > 420$ nm, 220μ m/cm², 5μ min). Cell viability of A549 cells at different concentrations of $1 \cdot 4CI$ (e) without and (f) with light irradiation. (g) Comparison of the viability of A549 cells treated by PEM, $1 \cdot PEG$, PEM@ $1 \cdot PEG$ with and without light irradiation (the concentrations of PEM were used as standard). Error bars denote the standard deviation (S.D., n = 3) ($\lambda = 450 \mu$ n, 10μ m/cm²).

1.4Cl could overlap with the mitochondria-labeling agent to a large extent, and the Pearson correlation coefficient (ρ) was obtained as high as 0.87, indicative of its mitochondrion-targeting ability (Supporting Information Figure S46). More interestingly, there is a

photoinduced intracellular translocation behavior of $1\cdot 4\text{Cl}$; that is, as shown in Figure 7b, when the A549 cells were incubated with $1\cdot 4\text{Cl}$ and then subjected to light irradiation with the xenon lamp, $1\cdot 4\text{Cl}$ was mainly distributed in the nucleus (ρ = 0.94 in Supporting



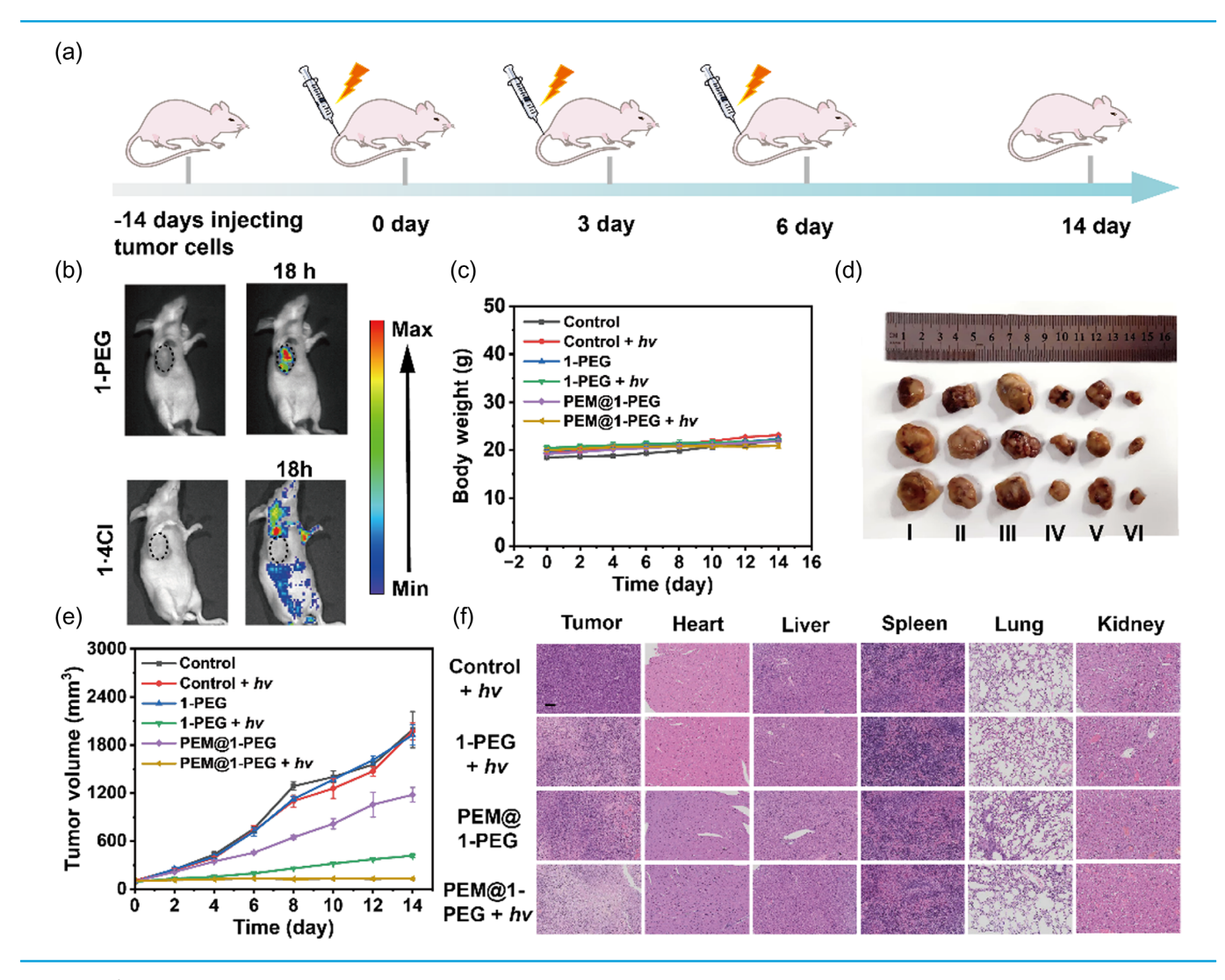


Figure 8 | (a) Overview of the in vivo antitumor experiments. (b) In vivo fluorescence imaging of the A549 tumor-bearing nude mice at 18 h after intravenous injection of $1 \cdot 4CI$ and $1 \cdot PEG$. (c) Body weight of mice with different treatments on day 14. Data were presented as mean \pm S.D. (n = 3). (d) Photographs of tumors collected from different treatments on day 14. (e) Tumor volumes of mice with treatments over different periods. Data were presented as mean \pm S.D. (n = 3). (f) Histological observation of the tumor tissues after different treatments. The tumor sections were stained with H&E. The scale bar is 100 μ m.

Information Figure S47). More gratifyingly, benefiting from the two-photon absorption property of 1·4CI, the A549 cells could be lightened up when excited at both 440 and 880 nm (Supporting Information Figure S48). Meanwhile, similar cell-imaging performance was observed when the molecular skeleton of 1·4CI was equipped with PEG chains (Supporting Information Figure S49).

Furthermore, the probe DHE was used to characterize the $O_2^{-\bullet}$ production in cells. Strong red fluorescence was observed after incubation with $1 \cdot 4CI$ in the A549 cells, which was consistent with the fluorescence signals arising from the reaction between DHE and superoxide species (Figure 7c). Moreover, DCFH-DA was also used as an indicator to detect the total ROS production in the

A549 cells. Bright green fluorescence was clearly observed, indicating that **1·4Cl** could produce a large amount of ROS after light irradiation (Figure 7c). The intracellular ROS generation by **1**-PEG was also assessed (Supporting Information Figure S50). Since **1·4Cl** could selectively accumulate in mitochondria, the mitochondrial membrane potential assay kit with JC-1 dye was used to detect the membrane potential changes caused by photosensitization in cells. At normal membrane potentials, JC-1 was aggregated as J-aggregates in the mitochondrial matrix, which could show red fluorescence. However, at low membrane potentials, JC-1 could not accumulate in the mitochondrial matrix and exist as monomers with green fluorescence. In our case, enhanced green fluorescence was clearly observed in all



the experimental groups compared to unilluminated ones, thus indicating that sufficient ROS generated by 1 · 4Cl could severely disrupt mitochondrial functions and eventually induce cell death (Figure 7d). The membrane potential changes of A549 cells incubated with 1-PEG and PEM@1-PEG were also examined (Supporting Information Figures S51 and S52). Notably, the presence of PEM resulted in more severe mitochondrial damage, mainly due to the synergistic outcomes of chemotherapeutic drugs and photodynamic treatment. Meanwhile, the oxidation ability of 1.4Cl toward the intercellular biomolecules was evaluated by measuring the intracellular NADH and BH₄ contents. The results showed that levels of both NADH and BH4 dramatically decreased in the 1-treated cells with light illumination, whereas this reduction was not observed in nonirradiated cells (Supporting Information Figures S53 and S54).

Finally, the viability of A549 cells was evaluated using CCK-8. As discerned from Figure 7e, $1\cdot 4CI$ alone showed negligible cytotoxicity even at 20 μ M with a half maximal inhibitory concentration (IC₅₀) of 54.95 μ M in the absence of light irradiation. In sharp contrast, the photocytotoxicity of $1\cdot 4CI$ greatly increased with an IC₅₀ value as low as only 2.26 μ M (Figure 7f). More satisfactorily, the PEGylated and drug-loaded nanoassembly gave the most significant photocytotoxicity among all the examined groups by the synergistic action of photosensitization and drug release in cells (Figure 7g and Supporting Information Table S3).

Since PEM@1-PEG exhibited excellent photoinduced toxicity at the cellular level, the tumor-bearing BALB/c mice were used as animal models to evaluate the antitumor efficacy by the subcutaneous injection of A549 cells (Figure 8a). After tumor implantation for 14 days, the in vivo enrichment effect was comparatively studied after the intravenous injection of 1·4Cl and 1-PEG into the tail vein of mice. As can be seen from Figure 8b, 1-PEG exhibited good enrichment at the tumor site over 18 h, whereas 1·4Cl alone showed no tumor targeting ability at the same time and weak fluorescence spread all over the mouse's body. These results confirm that PEGylation is a feasible approach to endow 1 with the desired targeting ability and prolong its retention in tumors.

Next, the mice were randomly divided into six groups (three mice per group) for in vivo anticancer experiments. During the 14-day treatment period, the mice's body weight slightly increased, and there was no significant difference among all the examined groups, indicating that none of the treatments caused systemic toxicity and possessed high biosafety (Figure 8c). The changes in tumor volumes were also monitored after mice sacrifice on the 14th day, showing that no obvious antitumor effect was observed for control groups or 1-PEG without light irradiation, while the tumor growth was significantly inhibited by the coinjection of PEGylated PSs and drug molecules upon exposure to light with the tumor

inhibition rate of 93.4% (Figure 8d,e). Additionally, histological analysis of the main organs (heart, liver, spleen, lung, and kidney) using the H&E staining method revealed no significant tissue damage in any of these main organs, indicating that the resultant nanoassembly could not cause irreparable harm to nontumor tissues and has good biocompatibility (Figure 8f). Comparatively, tumor tissue sections showed noticeable damage by the treatments of "1-PEG + $h\nu$ ", and "PEM@1-PEG", and "PEM@1-PEG + $h\nu$ " groups, which was consistent with the TGI results. The obtained data once again substantiate that the combined usage of macrocyclic PS and chemotherapeutic agent gave the most pronounced curative effect on tumor ablation.

Conclusion

In summary, a highly π -conjugated macrocyclic PS **1** · **4Cl** was rationally created by a readily accessible cyclization process and the photochemical mechanisms underlying the photocatalytic cascade reactions were fully elucidated using spectroscopic analysis and computational simulation. Benefiting from the positively charged macrocyclic structure, 1.4Cl can strongly bind the chemotherapeutic drug PEM. The covalent adornment of 1 · 4Cl with two PEG arms via hydrazone bonds allows the desired pH sensitivity to acidic microenvironment and the prolonged retention in tumors after intravenous administration and blood circulation. The photodynamic performance of macrocycle 1 · 4Cl matches the high criteria of an ideal PS, including good photostability, augmented fluorescence emission, two-photon absorption, and ROS generation simultaneously via Type-I/II pathways. Superior to most of the reported photodynamic agents, 1.4Cl gave exceptionally high 102 production efficiency. Notably, 1.4Cl can also photo-oxidize intracellular NADH and BH₄ by means of O₂-independent photoredox reactions. This results in significant cytotoxicity toward cancer cells, through aggravating redox imbalance in cells. In vivo studies corroborated the therapeutic efficacy of PEM@1-PEG to inhibit tumor growth in mice with satisfactory biosafety issues. Given the growing interest in supramolecular nanomedicine for basic research and clinical settings, our findings demonstrate the promising utility of nanoformulated macrocyclic PSs for diagnostic and therapeutic applications.

Disclosures

All experimental procedures were approved and in accordance with China's National Code of Animal Care for Scientific Experimentation. The experiments were also assessed by the Animal Experimentation Ethics Committee of Nankai University, and the assigned approval number is 2021-SYDWLL-000079.



Supporting Information

Supporting Information is available and includes synthesis of compounds, and other supplementary results.

Conflict of Interest

There is no conflict of interest to report.

Funding Information

This work is financially supported by the National Natural Science Foundation of China (grant nos. 22371148, 22171148, and 22131008), Haihe Laboratory of Sustainable Chemical Transformation, and the Fundamental Research Funds for the Central Universities (Nankai University).

Acknowledgments

We thank Dr. Yifu Chen at the College of Chemistry and Molecular Engineering of Peking University for crystallographic analysis. We thank the National Nature Science Foundation of China (grant nos. 22371148, 22171148, and 22131008), Haihe Laboratory of Sustainable Chemical Transformation, and the Fundamental Research Funds for the Central Universities (Nankai University) for financial support.

References

- 1. Feng, G.; Zhang, G.-Q.; Ding, D. Design of Superior Phototheranostic Agents Guided by Jablonski Diagrams. *Chem. Soc. Rev.* **2020**, *49*, 8179–8234.
- 2. Cheng, H.-B.; Li, Y.; Tang, B. Z.; Yoon, J. Assembly Strategies of Organic-Based Imaging Agents for Fluorescence and Photoacoustic Bioimaging Applications. *Chem. Soc. Rev.* **2020**, *49*, 21-31.
- 3. Nestoros, E.; Sharma, A.; Kim, E.; Kim, J. S.; Vendrell, M. Smart Molecular Designs and Applications of Activatable Organic Photosensitizers. *Nat. Rev. Chem.* **2024**, *9*, 46-60.
- 4. Nisa, K.; Lone, I. A.; Arif, W.; Singh, P.; Rehmen, S. U.; Kumar, R. Applications of Supramolecular Assemblies in Drug Delivery and Photodynamic Therapy. *RSC Med. Chem.* **2023**, *14*, 2438–2458.
- 5. Sowa, A.; Voskuhl, J. Host-Guest Complexes Boosting the Performance of Photosensitizers. *Int. J. Pharm.* **2020**, *586*, 119595.
- 6. Teng, K.-X.; Niu, L.-Y.; Yang, Q.-Z. A Host-Guest Strategy for Converting the Photodynamic Agents from a Singlet Oxygen Generator to a Superoxide Radical Generator. *Chem. Sci.* **2022**, *13*, 5951-5956.
- 7. Yang, K.; Zhang, Z.; Du, J.; Li, W.; Pei, Z. Host-Guest Interaction Based Supramolecular Photodynamic Therapy Systems: A Promising Candidate in the Battle Against Cancer. *Chem. Commun.* **2020**, *56*, 5865–5876.

- 8. Yuan, B.; Wu, H.; Wang, H.; Tang, B.; Xu, J.-F.; Zhang, X. A Self-Degradable Supramolecular Photosensitizer with High Photodynamic Therapeutic Efficiency and Improved Safety. *Angew. Chem. Int. Ed.* **2021**, *60*, 706–710.
- 9. Alvarez, N.; Sevilla, A. Current Advances in Photodynamic Therapy (PDT) and the Future Potential of PDT-Combinatorial Cancer Therapies. *Int. J. Mol. Sci.* **2024**, *25*, 1023.
- 10. Correia, J. H.; Rodrigues, J. A.; Pimenta, S.; Dong, T.; Yang, Z. Photodynamic Therapy Review: Principles, Photosensitizers, Applications, and Future Directions. *Pharmaceutics* **2021**, *13*, 1332.
- 11. Kataoka, H.; Nishie, H.; Hayashi, N.; Tanaka, M.; Nomoto, A.; Yano, S.; Joh, T. New Photodynamic Therapy with Next-Generation Photosensitizers. *Ann. Transl. Med.* **2017**, *5*, 183.
- 12. Zhao, X.; Liu, J.; Fan, J.; Chao, H.; Peng, X. Recent Progress in Photosensitizers for Overcoming the Challenges of Photodynamic Therapy: From Molecular Design to Application. *Chem. Soc. Rev.* **2021**, *50*, 4185-4219.
- 13. Zhou, Z.; Song, J.; Nie, L.; Chen, X. Reactive Oxygen Species Generating Systems Meeting Challenges of Photodynamic Cancer Therapy. *Chem. Soc. Rev.* **2016**, *45*, 6597–6626.
- 14. Zhou, Z.; Zhang, L.; Zhang, Z.; Liu, Z. Advances in Photosensitizer-Related Design for Photodynamic Therapy. *Asian J. Pharm. Sci.* **2021**, *16*, 668-686.
- 15. Dolmans, D. E. J. G. J.; Fukumura, D.; Jain, R. K. Photodynamic Therapy for Cancer. *Nat. Rev. Cancer* **2003**, *3*, 380-387.
- 16. Lucky, S. S.; Soo, K. C.; Zhang, Y. Nanoparticles in Photodynamic Therapy. *Chem. Rev.* **2015**, *115*, 1990-2042.
- 17. Pham, T. C.; Nguyen, V.-N.; Choi, Y.; Lee, S.; Yoon, J. Recent Strategies to Develop Innovative Photosensitizers for Enhanced Photodynamic Therapy. *Chem. Rev.* **2021**, *121*, 13454–13619.
- 18. Chen, D. P.; Xu, Q.; Wang, W. J.; Shao, J. J.; Huang, W.; Dong, X. C. Type I Photosensitizers Revitalizing Photodynamic Oncotherapy. *Small* **2021**, *17*, 2006742.
- 19. Hu, X.; Fang, Z.; Sun, F.; Zhu, C.; Jia, M.; Miao, X.; Huang, L.; Hu, W.; Fan, Q.; Yang, Z.; Huang, W. Deciphering Oxygen-Independent Augmented Photodynamic Oncotherapy by Facilitating the Separation of Electron-Hole Pairs. *Angew. Chem. Int. Ed.* **2024**, *63*, e202401036.
- 20. Teng, K.-X.; Niu, L.-Y.; Xie, N.; Yang, Q.-Z. Supramolecular Photodynamic Agents for Simultaneous Oxidation of NADH and Generation of Superoxide Radical. *Nat. Commun.* **2022**, *13*, 6179.
- 21. Yao, Q.; Fan, J.; Long, S.; Zhao, X.; Li, H.; Du, J.; Shao, K.; Peng, X. The Concept and Examples of Type-III Photosensitizers for Cancer Photodynamic Therapy. *Chem* **2022**, *8*, 197-209.
- 22. Yao, Q.; Li, H.; Xian, L.; Xu, F.; Xia, J.; Fan, J.; Du, J.; Wang, J.; Peng, X. Differentiating RNA from DNA by a Molecular Fluorescent Probe Based on the "Door-Bolt" Mechanism Biomaterials. *Biomaterials* **2018**, *177*, 78–87.
- 23. Dai, X.; Huo, M.; Zhang, B.; Liu, Z.; Liu, Y. Folic Acid-Modified Cyclodextrin Multivalent Supramolecular



- Assembly for Photodynamic Therapy. *Biomacromolecules* **2022**, *23*, 3549–3559.
- 24. Dai, X.; Zhang, B.; Zhou, W.; Liu, Y. High-Efficiency Synergistic Effect of Supramolecular Nanoparticles Based on Cyclodextrin Prodrug on Cancer Therapy. *Biomacromolecules* **2020**, *21*, 4998–5007.
- 25. Feng, H.-T.; Li, Y.; Duan, X.; Wang, X.; Qi, C.; Lam, J. W. Y.; Ding, D.; Tang, B. Z. Substitution Activated Precise Phototheranostics Through Supramolecular Assembly of AlEgen and Calixarene. *J. Am. Chem. Soc.* **2020**, *142*, 15966-15974. 26. Ma, H.; Xu, W.; Tang, X.; Kang, Y.; Xu, J.-F.; Zhang, X. A Supramolecularly Activatable Photosensitizer: Controllable Cyanine J-Aggregation for Efficient Photodynamic Therapy. *CCS Chem.* **2025**, *7*, 832-842.
- 27. Tang, M.; Liu, Y.-H.; Liu, H.; Mao, Q.; Yu, Q.; Kitagishi, H.; Zhang, Y.-M.; Xiao, L.; Liu, Y. Supramolecular Dual Polypeptides Induced Tubulin Aggregation for Synergistic Cancer Theranostics. *J. Med. Chem.* **2022**, *65*, 13473–13481.
- 28. Tang, M.; Song, Y.; Lu, Y.-L.; Zhang, Y.-M.; Yu, Z.; Xu, X.; Liu, Y. Cyclodextrin-Activated Porphyrin Photosensitization for Boosting Self-Cleavable Drug Release. *J. Med. Chem.* **2022**, *65*, 6764–6774.
- 29. Dong, X.; Dai, X.; Li, G.; Zhang, Y.-M.; Xu, X.; Liu, Y. Conformationally Confined Emissive Cationic Macrocycle with Photocontrolled Organelle-Specific Translocation. *Adv. Sci.* **2022**, *9*, 2201962.
- 30. Gao, Z.; Zheng, X.; Dong, X.; Liu, W.; Sha, J.; Bian, S.; Li, J.; Cong, H.; Lee, C.-S.; Wang, P. A General Strategy for Enhanced Photodynamic Antimicrobial Therapy with Perylenequinonoid Photosensitizers Using a Macrocyclic Supramolecular Carrier. *Adv. Healthcare Mater.* **2024**, *13*, 2401778.
- 31. Zheng, X.; Lei, S.-N.; Gao, Z.; Dong, X.; Xiao, H.; Liu, W.; Tung, C.-H.; Wu, L.-Z.; Wang, P.; Cong, H. Supramolecular Photosensitizers Using Extended Macrocyclic Hosts for Photodynamic Therapy with Distinct Cellular Delivery. *Chem. Sci.* **2023**, *14*, 3523–3530.
- 32. Inoue, Y.; Yamamoto, K.; Wada, T.; Everitt, S.; Gao, X.-M.; Hou, Z.-J.; Tong, L.-H.; Jiang, S.-K.; Wu, H.-M. Inclusion Complexation of (Cyclo)alkanes and (Cyclo)alkanols with 6-O-Modified Cyclodextrins. *J. Chem. Soc., Perkin Trans.* 2 **1998**, 1807–1816.
- 33. Zhao, S.; Zhang, L.; Deng, L.; Ouyang, J.; Xu, Q.; Gao, X.; Zeng, Z.; Liu, Y.-N. NIR-II Responsive Hydrogel as an Angiogenesis Inhibition Agent for Tumor Microenvironment Reprogramming. *Small* **2021**, *17*, 2103003.
- 34. Kale, A. A.; Torchilin, V. P. "Smart" Drug Carriers: PEGylated TATp-Modified pH-Sensitive Liposomes. *J. Liposome Res.* **2007**, *17*, 197–203.
- 35. Kang, H.; Rho, S.; Stiles, W. R.; Hu, S.; Baek, Y.; Hwang, D. W.; Kashiwagi, S.; Kim, M. S.; Choi, H. S. Size-Dependent EPR Effect of Polymeric Nanoparticles on Tumor Targeting. *Adv. Healthcare Mater.* **2020**, *9*, 1901223.
- 36. Mei, L.; Fu, L.; Shi, K.; Zhang, Q.; Liu, Y.; Tang, J.; Gao, H.; Zhang, Z.; He, Q. Increased Tumor Targeted Delivery Using a Multistage Liposome System Functionalized with RGD, TAT and Cleavable PEG. *Int. J. Pharm.* **2014**, *468*, 26–38.

- 37. Fang, Y.; Xue, J.; Gao, S.; Lu, A.; Yang, D.; Jiang, H.; He, Y.; Shi, K. Cleavable PEGylation: A Strategy for Overcoming the "PEG Dilemma" in Efficient Drug Delivery. *Drug Deliv.* **2017**, *24*, 22–32.
- 38. Kanamala, M.; Palmer, B. D.; Jamieson, S. M. F.; Wilson, W. R.; Wu, Z. Dual pH-Sensitive Liposomes with Low pH-Triggered Sheddable PEG for Enhanced Tumor-Targeted Drug Delivery. *Nanomedicine* **2019**, *14*, 1972–1990.
- 39. Sun, F.; Zhao, W.; Shen, H.; Fan, N.; Zhang, J.; Liu, Q.; Xu, C.; Luo, J.; Zhao, M.; Chen, Y.; Lam, K. W. K.; Yang, X.; Kwok, R. T. K.; Lam, J. W. Y.; Sun, J.; Zhang, H.; Tang, B. Z. Design of Smart Aggregates: Toward Rapid Clinical Diagnosis of Hyperlipidemia in Human Blood. *Adv. Mater.* **2022**, *34*, 2207671. 40. Zheng, X.; Peng, Q.; Zhu, L.; Xie, Y.; Huang, X.; Shuai, Z. Unraveling the Aggregation Effect on Amorphous Phase AIE Luminogens: A Computational Study. *Nanoscale* **2016**, *8*, 15173–15180.
- 41. Li, J.; Zhang, J.; Wang, J.; Wang, D.; Yan, Y.; Huang, J.; Tang, B. Z. Insights into Self-Assembly of Nonplanar Molecules with Aggregation-Induced Emission Characteristics. *ACS Nano* **2022**, *16*, 20559–20566.
- 42. Zhang, J.; Tu, Y.; Shen, H.; Lam, J. W. Y.; Sun, J.; Zhang, H.; Tang, B. Z. Regulating the Proximity Effect of Heterocycle-Containing AlEgens. *Nat. Commun.* **2023**, *14*, 3772.
- 43. Berezin, M. Y.; Achilefu, S. Fluorescence Lifetime Measurements and Biological Imaging. *Chem. Rev.* **2010**, *110*, 2641–2684.
- 44. He, G. S.; Tan, L.-S.; Zheng, Q.; Prasad, P. N. Multiphoton Absorbing Materials: Molecular Designs, Characterizations, and Applications. *Chem. Rev.* **2008**, *108*, 1245-1330.
- 45. Kim, H. M.; Cho, B. R. Small-Molecule Two-Photon Probes for Bioimaging Applications. *Chem. Rev.* **2015**, *115*, 5014-5055.
- 46. Yu, H.-J.; Zhou, Q.; Dai, X.; Shen, F.-F.; Zhang, Y.-M.; Xu, X.; Liu, Y. Photooxidation-Driven Purely Organic Room-Temperature Phosphorescent Lysosome-Targeted Imaging. *J. Am. Chem. Soc.* **2021**, *143*, 13887-13894.
- 47. Zhou, X.; Bai, X.; Shang, F.; Zhang, H.-Y.; Wang, L.-H.; Xu, X.; Liu, Y. Supramolecular Assembly Activated Single-Molecule Phosphorescence Resonance Energy Transfer for Near-Infrared Targeted Cell Imaging. *Nat. Commun.* **2024**, *15*, 4787.
- 48. Berbigier, J. F.; da Luz, L. C.; Rodembusch, F. S. Recent Advances in Thermally Activated Delayed Fluorescent Materials in Type II Photodynamic Therapy. *Chem. Rec.* **2024**, *24*, e202400146.
- 49. Prieto-Montero, R.; Sola-Llano, R.; Montero, R.; Longarte, A.; Arbeloa, T.; López-Arbeloa, I.; Martínez-Martínez, V.; Lacombe, S. Methylthio BODIPY as a Standard Triplet Photosensitizer for Singlet Oxygen Production: A Photophysical Study. *PCCP* **2019**, *21*, 20403–20414.
- 50. Nair, J. R.; McGuire, J. J. Submitochondrial Localization of the Mitochondrial Isoform of Folylpolyglutamate Synthetase in CCRF-CEM Human T-lymphoblastic Leukemia Cells. *Biochim. Biophys. Acta Mol. Cell. Res.* **2005**, *1746*, 38–44.
- 51. Rollins, K. D.; Lindley, C. Pemetrexed: A Multitargeted Antifolate. *Clin. Ther.* **2005**, *27*, 1343–1382.



- 52. Taylor, E. C.; Kuhnt, D.; Shih, C.; Rinzel, S. M.; Grindey, G. B.; Barredo, J.; Jannatipour, M.; Moran, R. G. A Dideazate-trahydrofolate Analogue Lacking a Chiral Center at C-6, *N*-[4-[2-(2-Amino-3,4-dihydro-4-oxo-7H-pyrrolo[2,3-d]pyrimidin-5yl)ethyl[benzoyl]-L-glutamic Acid, Is an Inhibitor of Thymidylate Synthase. *J. Med. Chem.* **1992**, *35*, 4450–4454. 53. Lakowicz, J. R. *Principles of Fluorescence Spectroscopy*; Springer US: New York, **2006**.
- 54. Gao, J.; Li, J.; Geng, W.-C.; Chen, F.-Y.; Duan, X.; Zheng, Z.; Ding, D.; Guo, D.-S. Biomarker Displacement Activation: A General Host-Guest Strategy for Targeted Phototheranostics in Vivo. *J. Am. Chem. Soc.* **2018**, *140*, 4945-4953.
- 55. Hossain, M. S.; Dietz, K. J. Tuning of Redox Regulatory Mechanisms, Reactive Oxygen Species and Redox Homeostasis Under Salinity Stress. *Front. Plant Sci.* **2016**, *7*, 548.
- 56. Huang, H.; Banerjee, S.; Qiu, K.; Zhang, P.; Blacque, O.; Malcomson, T.; Paterson, M. J.; Clarkson, G. J.; Staniforth, M.; Stavros, V. G.; Gasser, G.; Chao, H.; Sadler, P. J. Targeted Photoredox Catalysis in Cancer Cells. *Nat. Chem.* **2019**, *11*, 1041–1048
- 57. Lee, C. F.; Chavez, J. D.; Garcia-Menendez, L.; Choi, Y.; Roe, N. D.; Chiao, Y. A.; Edgar, J. S.; Goo, Y. A.; Goodlett, D. R.; Bruce, J. E.; Tian, R. Normalization of NAD⁺ Redox Balance as a Therapy for Heart Failure. *Circulation* **2016**, *134*, 883–894. 58. Baradaran, R.; Berrisford, J. M.; Minhas, G. S.; Sazanov, L. A. Crystal Structure of the Entire Respiratory Complex I. *Nature* **2013**, *494*, 443–448.
- 59. White, A. T.; Schenk, S. NAD⁺/NADH and Skeletal Muscle Mitochondrial Adaptations to Exercise. *Am. J. Physiol. Biochem. Pharmacol.* **2012**, *303*, E308–E321.
- 60. Zhang, Y.; Zhao, Y.; Li, R.; Liu, J. Bioinspired NADH Regeneration Based on Conjugated Photocatalytic Systems. *Sol. RRL* **2021**, *5*, 2000339.
- 61. Li, Q.; Yan, C.; Zhang, P.; Wang, P.; Wang, K.; Yang, W.; Cheng, L.; Dang, D.; Cao, L. Tetraphenylethene-Based Molecular Cage with Coenzyme FAD: Conformationally Isomeric Complexation Toward Photocatalysis-Assisted

- Photodynamic Therapy. *J. Am. Chem. Soc.* **2024**, *146*, 30933-30946.
- 62. Wang, Y.; Shen, H.; Li, Z.; Liao, S.; Yin, B.; Yue, R.; Guan, G.; Chen, B.; Song, G. Enhancing Fractionated Cancer Therapy: A Triple-Anthracene Photosensitizer Unleashes Long-Persistent Photodynamic and Luminous Efficacy. *J. Am. Chem. Soc.* **2024**, *146*, 6252-6265.
- 63. Maenaka, Y.; Suenobu, T.; Fukuzumi, S. Efficient Catalytic Interconversion Between NADH and NAD+ Accompanied by Generation and Consumption of Hydrogen with a Water-Soluble Iridium Complex at Ambient Pressure and Temperature. *J. Am. Chem. Soc.* **2012**, *134*, 367-374.
- 64. Crabtree, M. J.; Channon, K. M. Synthesis and Recycling of Tetrahydrobiopterin in Endothelial Function and Vascular Disease. *Nitric Oxide-Biol. Chem.* **2011**, *25*, 81-88.
- 65. Fanet, H.; Capuron, L.; Castanon, N.; Calon, F.; Vancassel, S. Tetrahydrobioterin (BH₄) Pathway: From Metabolism to Neuropsychiatry. *Curr. Neuropharmacol.* **2021**, *19*, 591-609.
- 66. Shi, W.; Meininger, C. J.; Haynes, T. E.; Hatakeyama, K.; Wu, G. Regulation of Tetrahydrobioterin Synthesis and Bioavailability in Endothelial Cells. *Cell Biochem. Biophys.* **2004**, *41*, 415-433.
- 67. Chen, W.; Wang, Z.; Tian, M.; Hong, G.; Wu, Y.; Sui, M.; Chen, M.; An, J.; Song, F.; Peng, X. Integration of TADF Photosensitizer as "Electron Pump" and BSA as "Electron Reservoir" for Boosting Type I Photodynamic Therapy. *J. Am. Chem. Soc.* **2023**, *145*, 8130–8140.
- 68. Teng, K.-X.; Zhang, D.; Liu, B.-K.; Liu, Z.-F.; Niu, L.-Y.; Yang, Q.-Z. Photo-Induced Disproportionation-Mediated Photodynamic Therapy: Simultaneous Oxidation of Tetrahydrobiopterin and Generation of Superoxide Radicals. *Angew. Chem. Int. Ed.* **2024**, *63*, e202318783.
- 69. Wang, X.; Peng, J.; Meng, C.; Feng, F. Recent Advances for Enhanced Photodynamic Therapy: From New Mechanisms to Innovative Strategies. *Chem. Sci.* **2024**, *15*, 12234–12257.